4. CW models guarantee 3D-like results and with a computational costs far lower than those required for the solid model, for the double cell case study in terms of DOFs for the solid model are more then 40 times greater then LE 1D model and more then thirty times greater then TE proposed 1D model;

5. The TE convergence analysis has been presented after that an appropriate choice of the approximation order allows to obtain more accurate results. $N = 8$ and the LE models provide the best accuracy with relevant improvements in the axial stress recovery;

6. The LE models proved to be the best accuracy/computational cost choice, for this reason this formulation has been chosen for failure analysis applications;

7. The present 1D formulation is extremely advantageous in terms of computational costs if compared with solid models.

8. The CW approach appears to be attractive in the perspective of a detailed analysis of more complex structural configurations. Cells can be opportunely included in order to refine the model in areas that were considered critical following preliminary analyses.

3.5 Cross-Ply Laminate

This section is devoted to the structural analysis of a cantilevered laminated beam. The geometry of this model is described in Figure 3.14. The length of the beam, L, is equal to

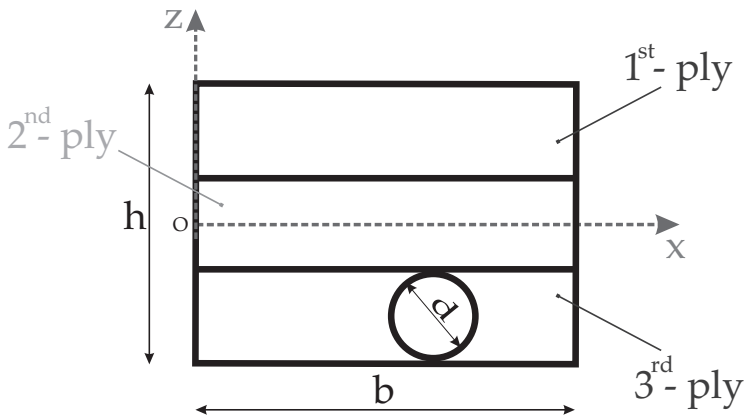

Figure 3.14. Geometry of the laminated plate.

40 mm, the height (h) and the width (b) are equal to 0.6 mm and 0.8 mm, respectively. Fibers were modeled as having a circular cross-section, the diameter, d, is equal to 0.2 mm. Four fibers per layer were considered. A point-load, F_z, was applied at $[b/2,\ L,\ 0]$, $F_z = -50$ N. Fibers were considered orthotropic, with $E_L = 202.038$ GPa, $E_T = E_z = 12.134$ GPa, $G_{LT} = 8.358$ GPa, $G_{Lz} = 8.358$ GPa, $G_{Tz} = 47.756$ GPa, $\nu_{LT} = 0.2128$, ν_{Lz}

= 0.2128 and $\nu_{Tz} = 0.2704$. An isotropic matrix was adopted, with $E = 3.252$ GPa and $\nu = 0.355$. Layer properties were the following: $E_L = 159.380$ GPa, $E_T = E_z = 14.311$ GPa, $G_{LT} = 3.711$ GPa, $G_{Lz} = 3.711$ GPa, $G_{Tz} = 5.209$ GPa, $\nu_{LT} = 0.2433$, $\nu_{Lz} = 0.2433$ and $\nu_{Tz} = 0.2886$. Figure 3.15 shows the modeling approaches considered for this analysis, both TE ($N = 4$) and LE were used for each model. In model 1, the three layers

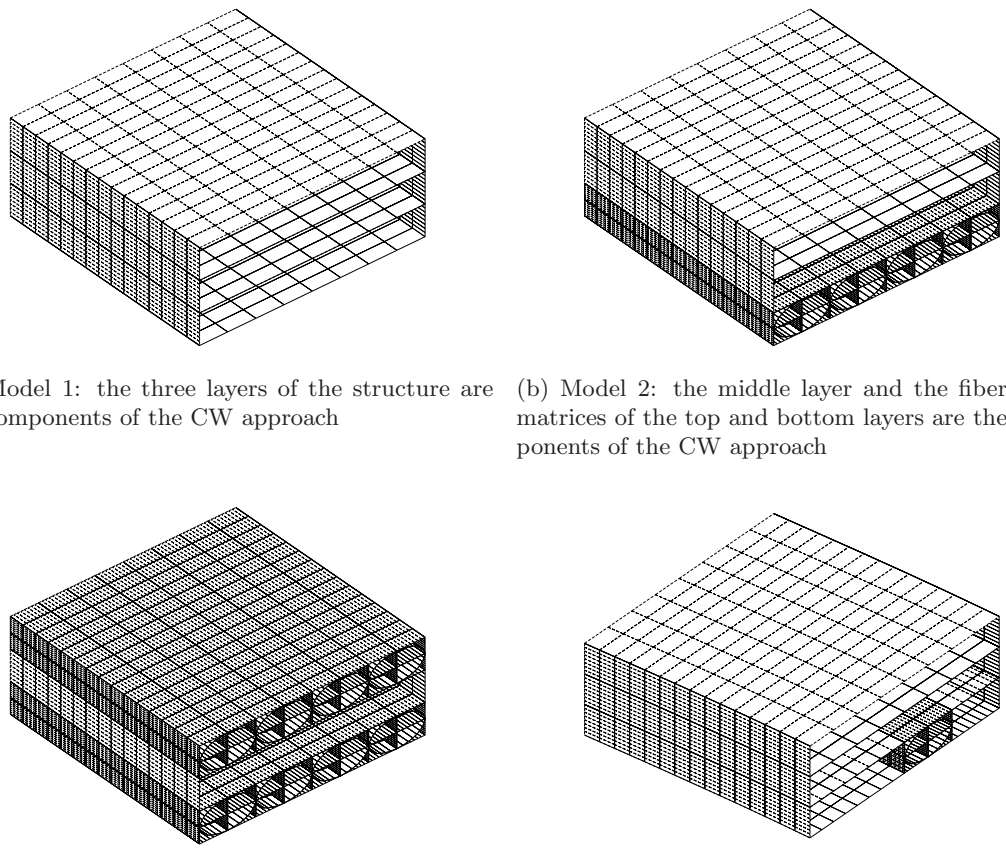

(a) Model 1: the three layers of the structure are the components of the CW approach

(b) Model 2: the middle layer and the fibers and matrices of the top and bottom layers are the components of the CW approach

(c) Model 3: the top and middle layers and the fibers and matrices of the bottom layer are the components of the CW approach

(d) Model 4: only one fiber-matrix cell is inserted in the CW model

Figure 3.15. Different modeling approaches for the laminate.

of the structure were considered as the components of the CW approach. In model 2, the middle layer and the fibers and matrices of the top and bottom layers were considered as components. Model 3 components are the top and middle layers and the bottom layer fibers and matrices. In Model 4, only one single fiber-matrix cell was considered.
Table 3.12 shows the transverse displacement of the loading point and the axial stress at the center point of the third fiber of the bottom layer. It is important to notice that this fiber is a component in Models 2, 3 and 4. Shear stress values are reported in Table 3.13 on two different points, A (matrix) and B (fiber). The axial stress along the thickness

Model	u_z mm	$\sigma_{yy} \times 10^{-2}$ MPa
	TE	
1	−9.630	−5.708
2	−10.223	−7.564
3	−9.921	−7.766
4	−9.675	−7.295
	LE	
1	−9.629	−5.758
2	−9.927	−7.495
3	−9.775	−7.418
4	−9.666	−7.264

Table 3.12. Transverse displacement, at $[b/2,\ L,\ 0]$, and axial stress, at $[0.5,\ 0,\ -0.2]$, of the laminate.

Model	σ^A_{XY}	σ^B_{XY}
1	1.579	0.363
2	0.512	0.641
3	0.513	0.660
4	1.569	0.716

Table 3.13. Shear stress, σ_{xy} MPa, at two different points of the laminate, A[0.8, 0, 0] and B [0.55, 0, −0.2], LE models.

direction is shown in Figure 3.16 where TE and LE solutions are superimposed. Shear

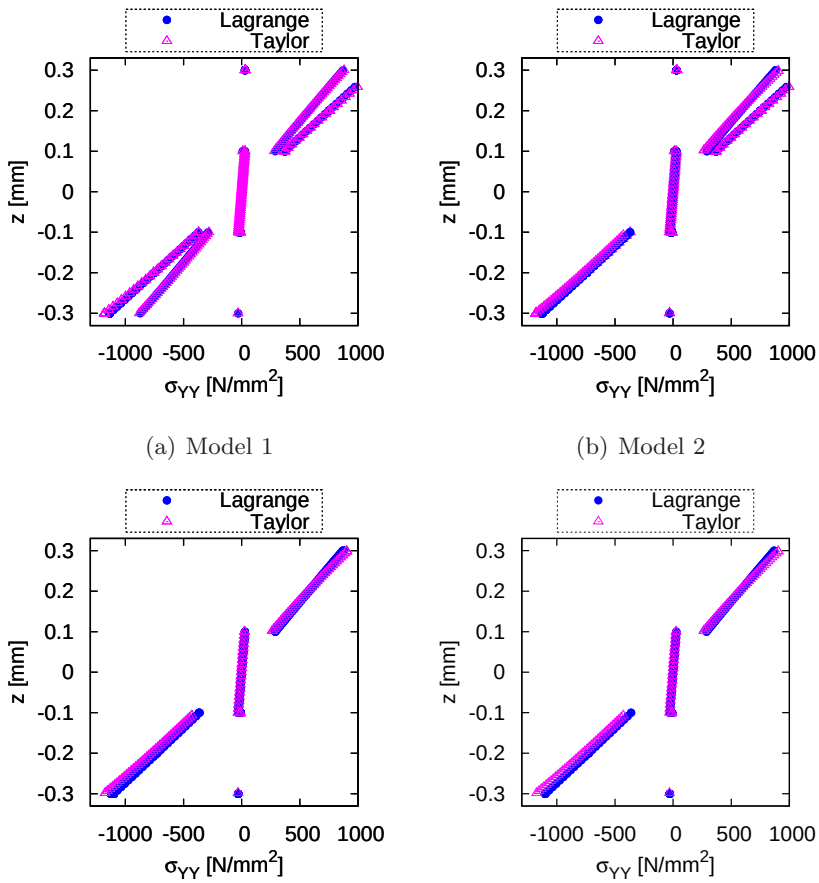

(a) Model 1

(b) Model 2

(c) Model 3

(d) Model 4

Figure 3.16. Axial stress σ_{yy} along z at $x = 0.3$, $y = 0.0$.

stress distributions above the clamped cross-section from LE models are given in Figure 3.17. Shear stress results are herein provided by means of LE models only, this is due to the better accuracy that LEs are able to obtain for shear as seen in Carrera and Petrolo [15]. The analysis of the results suggests the following:

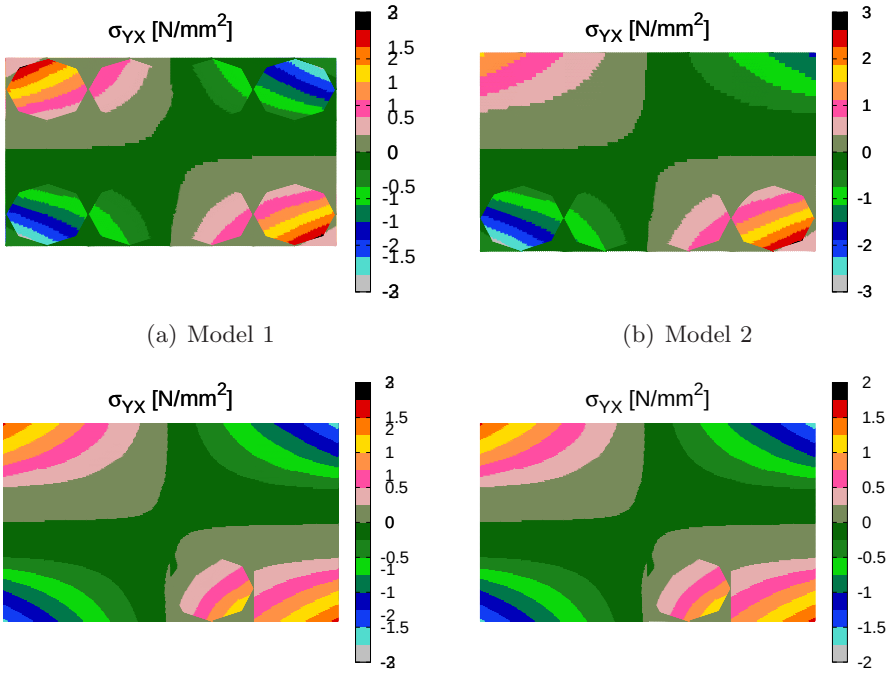

(a) Model 1 (b) Model 2

(c) Model 3 (d) Model 4

Figure 3.17. Shear stress, σ_{yx}, distribution above the cross-section at $y = 0$, laminated beam, LE models.

1. Stress fields, herein computed by means of the constitutive laws, are significantly affected by the choice of the modeling approach. Depending on the choice of the components, far different stress fields were detected. This because homogenized material characteristics were used for layers whereas the characteristics of each component were adopted for fibers and matrices. These differences are particularly relevant for the matrix stress values.

2. The adoption of localized fiber-matrix components (restricted to a lamina in Model 3 or to a fiber-matrix cell in Model 4) allows us to use simpler models without considerably affecting the accuracy of the result if compared to more cumbersome models. This means that, if an accurate stress field is needed around a given fiber, the use of fiber-matrix components can be limited to the fiber location.

3. Displacement values are less influenced than stress fields by the choice of the modeling approach. The peak value provided by TE in Model 2 is most likely due to the detection of local effects caused by the point load, the detection of this effect is one of the enhanced capability provided by refined CUF models. This is a known behavior from previous CUF works [14].

4. No significant differences were observed between TE and LE results, however, as general guideline, LEs should be preferred to TE if shear stresses have to be computed.

3.6 Composite C-Shaped Beam

This section is devoted to the analysis of a more complex composite structure composed by laminates and soft cores. The aim of this assessment is to exploit the capabilities of the present 1D component-wise formulation to analyze typical aeronautical structural components such as spars or longerons. A cantilevered beam is considered whose cross-section geometry is shown in Figure 3.18, the components of this structure are the following:

1. Two horizontal unidirectional (UD) top and bottom flanges.

2. A core made of foam.

3. Two $-45/+45$ vertical thin layers which coat the foam core.

Dimensions are given in Table 3.14, the length-to-height ratio, L/h, is equal to ten. Foam was considered isotropic with $E = 50$ MPa and $\nu = 0.25$. Vertical layers are orthotropic with $E_L = 40$ GPa, $E_T = 4$ GPa, $G = 1$ GPa, $\nu = 0.25$, the same Poisson and shear modulus values are used in all directions. UD flanges were modeled by means of four different configurations, as shown in Figs. 3.19; these figures also present the cross-section discretization adopted in the LE models. In the first case (Model 1), the components of the CW model are the UD flanges, the vertical thin layers and the soft core. Model 2 and 3 have one fiber-matrix cell. Model 4 has all the top flange modeled with fiber-matrix cells. The single cell geometry is shown in Figure 3.5, the geometrical data are the following: d

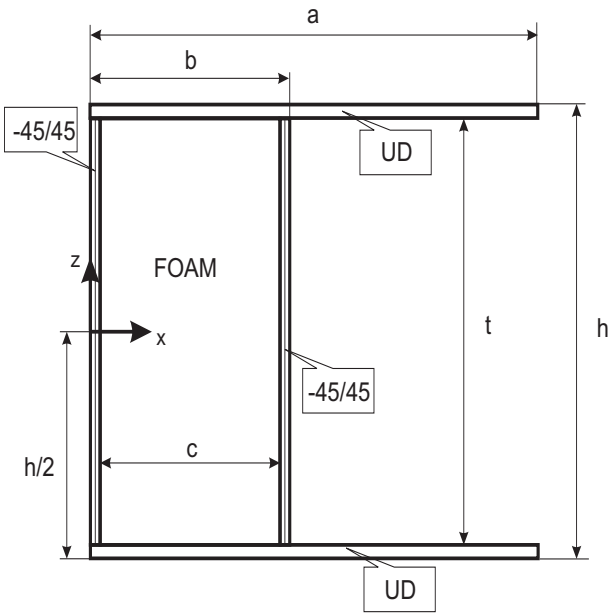

Figure 3.18. Geometry of the C-shaped cross-section.

	[mm]
a	18
b	9.4
c	8.6
h	18
t	17.4

Table 3.14. Cross-Section dimensions of the C-shaped cross-section.

$= b = 0.3$ mm. The material characteristics of fibers, matrix and homogenized laminae are the same of those seen in the laminated beam section. As first loading case, a unitary point load is applied at the bottom surface $[a/2,\ L,\ -h/2]$ along the z-direction, $F_z = -1$ N. Results were obtained by means of TE ($N = 4$) and LE models. The loading line does not cross the shear center as shown in Figure 3.20. Table 3.15 shows the transverse displacement of the loading point and Table 3.16 reports the axial stress in a point above the bottom flange at the clamped cross-section. Figures 3.21 and 3.22 show the free-tip transverse displacement distribution and stress distributions at the clamped cross-section, respectively. Stress distributions above the first fiber-matrix cell of the top flange are also given. As second loading case, two opposite unitary point loads are applied at $[a,\ L,\ \pm h/2]$ along the z-direction, $F_z = \pm 1$ N. In this case, only LE models were adopted since TE would require very high expansion orders to detect correct displacement fields as shown in [15]. Table 3.17 presents the transverse displacement of the top loading point. Figure 3.23 shows the 3D deformed configuration of the structure. The results obtained suggest the following:

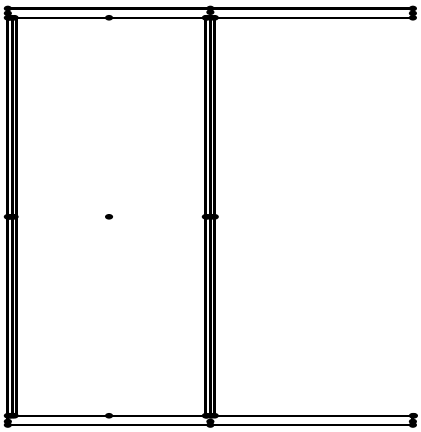

(a) Model 1

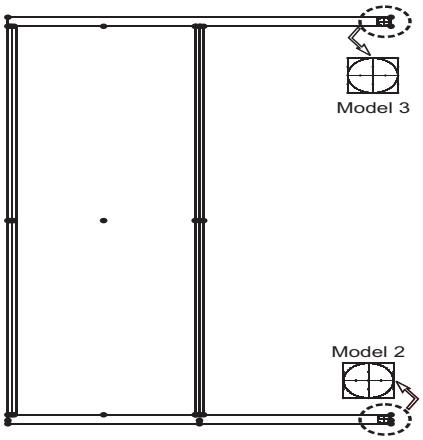

(b) Models 2 and 3

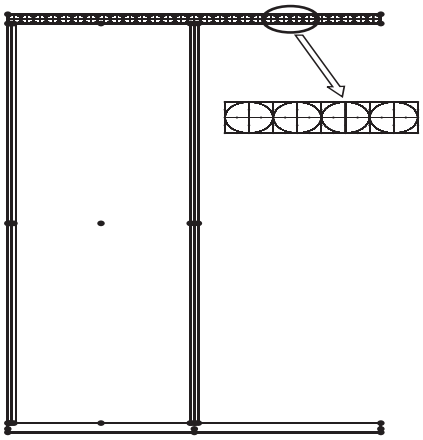

(c) Model 4

Figure 3.19. Description of the modeling approaches for the C-shaped beam.

Model	u_z
TE	
1	−1.907
2	−1.907
3	−1.907
4	−1.920
LE	
1	−2.000
2	−2.003
3	−2.003
4	−2.024

Table 3.15. Vertical displacement, $u_z \times 10^2$ mm, at the loading point of the C-shaped beam, first loading case.

Model	σ_{yy}
TE	
1	−2.177
2	−2.177
3	−2.175
4	−2.147
LE	
1	−2.283
2	−2.293
3	−2.282
4	−2.053

Table 3.16. Axial stress, $\sigma_{yy} \times 10^2$ MPa, at $[a/2,\ 0,\ -h/2]$, C-shaped beam, first loading case.

Model	u_z
1	1.161
2	1.211
3	1.071
4	1.130

Table 3.17. Vertical displacement, u_z [mm], at $[a,\ L,\ h/2]$, C-shaped beam, second loading case.

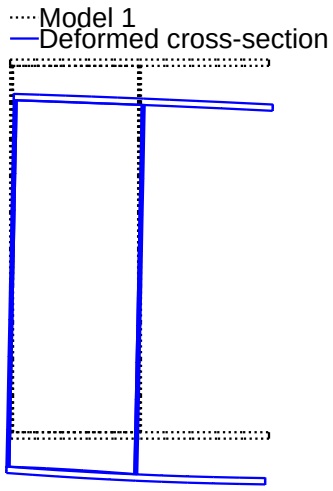

Figure 3.20. Deformed cross-sections of the Model 1.

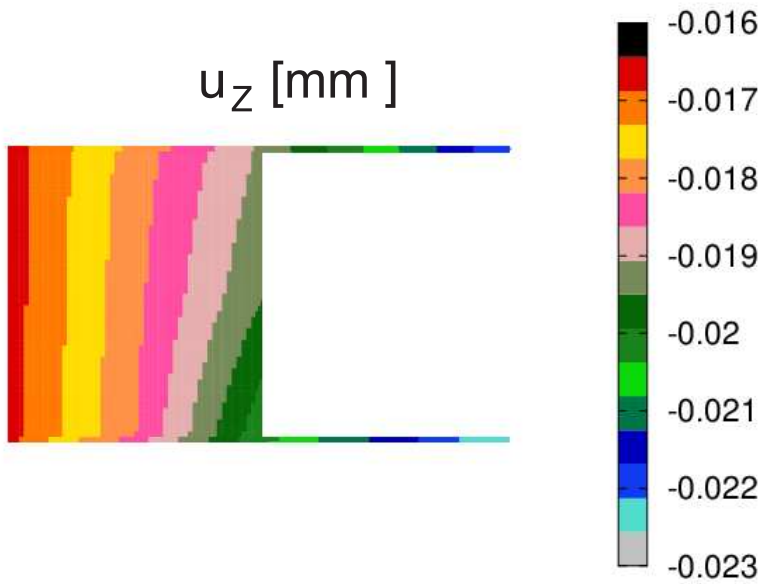

Figure 3.21. Transverse displacement distribution above the free-tip cross-section via Model 4, first loading case.

1. As far as the first loading case is concerned, LE models provide larger transverse displacements. This is due to the fact that a fourth-order TE models is not always enough to deal with thin walled and/or open cross-sections.

2. The different modeling approaches provide similar displacement values in the first loading case, whereas more significant differences were observed in the second loading

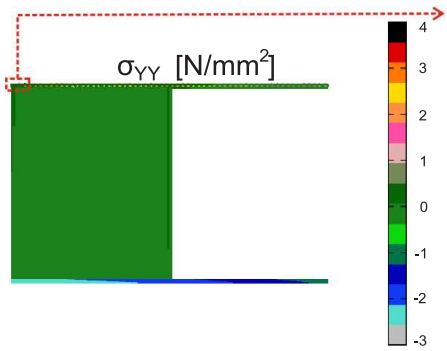

(a) Axial stress σ_{yy}

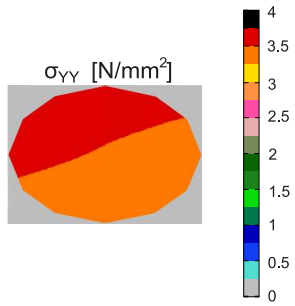

(b) Axial stress above a unit cell

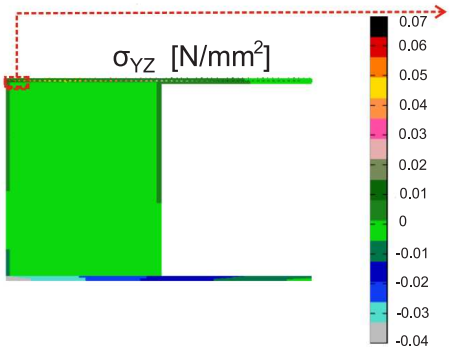

(c) Shear stress σ_{yz}

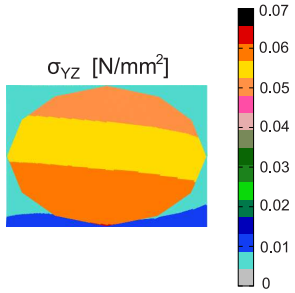

(d) Shear stress above a unit cell

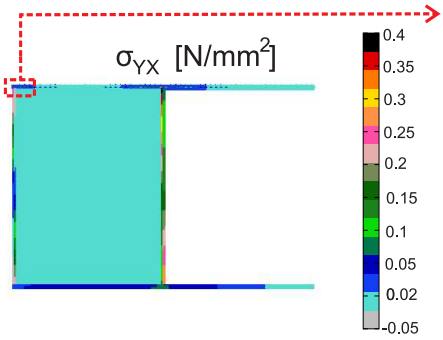

(e) Shear stress σ_{yx}

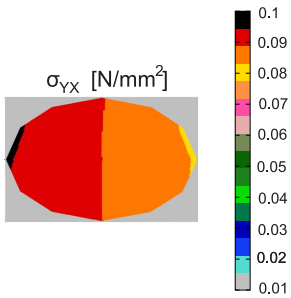

(f) Shear stress above a unit cell

Figure 3.22. Stress distributions above the C-shaped cross section at $y = 0$ via model 4, first loading case.

case. In particular, model 2 and 3 provided quite different values; this is most likely due to the local effect given by the different fiber-matrix modeling. In model 2, the

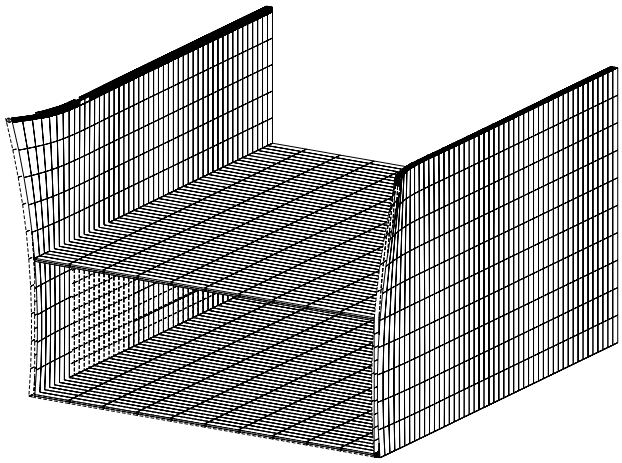

Figure 3.23. Deformed configuration of the C-shaped beam via model 2, second loading case.

point where the displacement was evaluated is in a layer portion of the structure with homogenized material characteristics. In model 3, the same point is in the fiber-matrix portion where the fiber plays a significant role in the local mechanical behavior of the structure.

3. It is confirmed that stress fields can be significant different if different components combinations are considered.

4. The present 1D formulation can detect accurate 3D displacement field of thin walled structures under point loads.

Different structural problems have been discussed in this chapter, including fiber-matrix cells, laminated beams and composite C-shaped beams. Compact and thin walled structures were considered under point loads and results were evaluated in terms of displacement and stress fields. Comparisons with solid models from commercial codes were provided. The results obtained suggest the following.

1. The proposed CW approach offers significant improvements in detecting the mechanical behavior of laminated structures in particular when stress fields around fiber and matrix cells have to be accurately computed.

2. If only layers are considered as components of a composite structure, far different stress fields could be detected if compared to those by a model including the real geometrical and material characteristics of fibers and matrices.

3. The present 1D formulation is extremely convenient in terms of computational costs if compared to solid models. Moreover, a global-local approach can be easily implemented since the same stiffness matrix is adopted to model each component of the structure.

Chapter 4

The CW approach for the evaluation of integral quantities

In chapter 3 has been shown that the CW approach allows the modelling of a fiber-reinforced composite structure up to the component scale. Has been proved that this technique has enhanced structural capabilities to detect accurate stress/strain fields in the matrix, fibers, layers and interfaces of composite layered structures with low computational costs. Numerical results on different structural problems have also been presented. The present chapter proposes to exploit this approach to evaluate integral quantities to identify potential critical areas of a composite structure.

4.1 Introduction

Fiber reinforced laminates, textile laminates and sandwich structures are some of the composite configurations increasingly used in many engineering applications. Because of their layup, characterizing their mechanical behavior require to take into account different components at different scales and usually involves advanced analysis tools. As introduced in chapter 6 these interfaces can determine many different failure modes. If multiscales approches are used, it is actually possible to properly model the composite structure components and estimate representative parameters to characterize their behaviour in critical components or critical portion of the structure. As for traditional matallic materials, integral quantities can be interesting parameters to predict failure of cracked bodies. As shown in Figure 4.1, depending on the failure mode to be modeled, interfaces can be lines, areas or volumes and then 1D-, 2D- and 3D- integrals have to be computed. In fact, reaction forces exchanged through the tickness can lead to delamination while if the fiber/matrix interface is taken into account the debonding/pull-out can be analyzed. For the microcracks analysis line countours can be taken into account. In this perspective, the J integral method has been introduced for the analysis of metallic structure and has received much attention due to its several attractive features. Thee path indipendent J integral, formulated by Rice [49], can be viewed as a parameter which is an average measure of the crack tip elastic-plastic field. In subsequent works Rice [50] shown that the

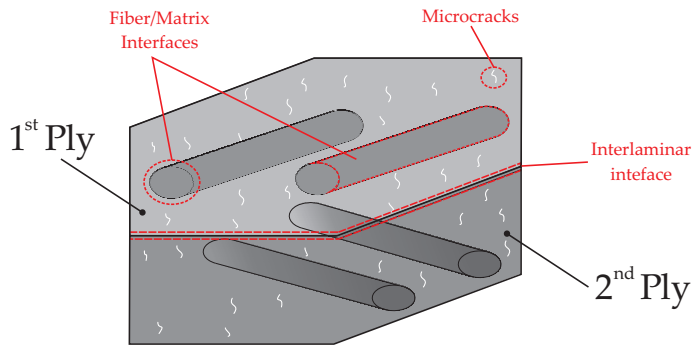

Figure 4.1. Typical component interfaces for composite laminates.

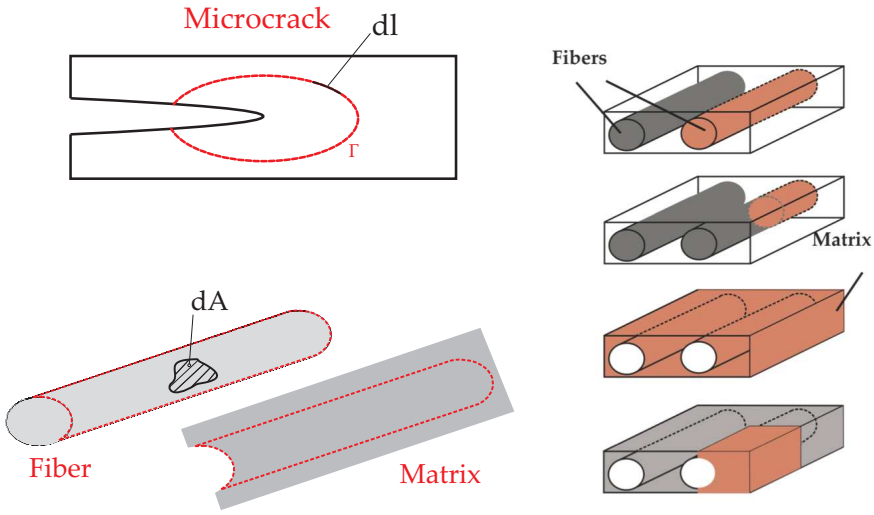

Figure 4.2. 1D-, 2D- and 3D-subdomains for the evaluation of integral failure parameters.

J-integral can be directly evaluated from single load-displacement records, that makes this value attractive to be used as elastic-plastic fracture criterion [51]. A wide range of application of the J-integral approach can be found in literature, indeed has been deduced that the J-integral approach is a very powerful tool when the fracture mechanics assumptions lose their validity, i.e. crack dimension in the same scale of component sizes, or when the singularities into the stress and strain fields are included into the model. A possible extension for three-dimensional problems has been presented by Kishimoto [52] and possible application of the J-integral method as fracture criterion has been discussed. Catalanotti et Al. [53] use the J integral method in a new methodology to mesure the crack resistance curves (R-curve) for fiber-dominated failure modes in polymer-matrix composites that allow to characterize the fracture toughness of the considered material and to evaluate the parameters used in softening laws for the numerical simulation of the fracture mechanism. The fracture toughness (G_{IC}) play a key role in determining the composite response during damage propagation. For composite materials, Pinho et Al. [54] use the J-integral

method to determine the fracture toughnesses of the tensile and compressive fibre failure modes in laminated composites. Furthermore, the path-independent J integral can be used for characterising the failure process zone when the linear elastic fracture mechanics (LEFM) approximations are not valid as proposed by Sørensena and Jacobsenb for the determination of cohesive laws to describe large scale failure [55] a similar approach was alredy presented by Li and Ward [56] for cementitious composites.

4.2 Integral quantities

First, the strain energy is evaluated as integral parameter in order to have a solid validation of results. The strain energy E_i is obtained via the Principle of Virtual Displacements

$$E_i = \int_{V_i} \boldsymbol{\sigma}^T \boldsymbol{\epsilon} \; dV_i \tag{4.1}$$

where $E_{i,ax}$ is the component of the strain energy related to the axial strain and stress and $E_{i,s}$ is related to the shear components yz, xy.

$$E_{i,ax} = \int_{V_i} \sigma_{yy}\epsilon_{yy} \; dV_i, \qquad E_{i,s} = \int_{V_i} (\sigma_{yz}\epsilon_{yz} + \sigma_{xy}\epsilon_{xy}) \; dV_i \tag{4.2}$$

Respectively referred to as axial and shear strain energies in the following sections. In composite structures, failure can occurs due to fiber or matrix collapse, debonding or delamination. To determine where failure occurs, integral quantities can be evaluated in subdomains that can be lines, areas or volumes of the components or at lamina/fiber-matrix interfaces. After a preliminary analysis at the macroscale level, the model capabilities can be tuned by choosing in which portion of the structure a more detailed model has to be used. In other words, detailed models can be progressively obtained up to the fiber and matrix subvolume dimensions to identify which part of the structure is working in the most critical conditions. Failure index offers a punctual evaluation of the criticality in a given structure. To overcome the puntual evaluation the CW integral approach is applied to evaluate a failure parameter related to subvolumes. Results are given in terms of FI_i^*

$$FI^* = \frac{\sum_{i=1}^{NVol} \frac{\int_{V_i} FI \; dV_i}{V_i}}{NVol} \tag{4.3}$$

where, FI_i^* is a function calculated as reported in eq.4.4 for a i-th subvolume.

$$FI_i^* = \frac{\int_{V_i} FI \; dV_i}{V_i} \tag{4.4}$$

Given a criterion, the corresponding FI is integrated in the subvolume dV_i and then normalized for the correspondind volume V_i. In order to obtain an evaluation on larger portions of the structure, subvolumes are combined and a further index is proposed in eq. 4.3 where the FI_i^* of each subvolume is summed and then normalised with respect to $NVol$

that is the total number of summed subvolumes. The index FI^* wants to be an example of evaluation of a failure parameters. Numerical results are herein discussed to show the capability of the present approach to analyse composite structures modelling at the same time components in different scales with a convenient computational cost. Examples have been carried out for different structural models. A homogeneous beam was considered as first assessment. Then, a single fiber-matrix cell was considered as simpliest case study in the CW perspective. Last, a multilayered beam was considered modelling the fist layer including fiber/matrix cells in different positions. Material is considered isotropic for the homogeneous case study with Young modulus,E, equal to 127.6 [GPa] and Poisson Ratio, ν, equal to 0.3. For the fiber and matrix materials, properties are reported in Table 6.5, chapter. Where for the failure coefficients, the subscripts T and C denote respectively the limit value in the case of tension and compression. Solid comparisons are provided.

4.2.1 Volume Integrals

In the FE framework, three dimensional integrals are usually evaluated in 3D analysis. Neverthenless, the 3D elements herein introduces are used just for post-processing purposes. The FE computation is performed with the 1D elements and at this level of the analysis unknowns at nodes have already been determined. Since we are using a 1D ele-

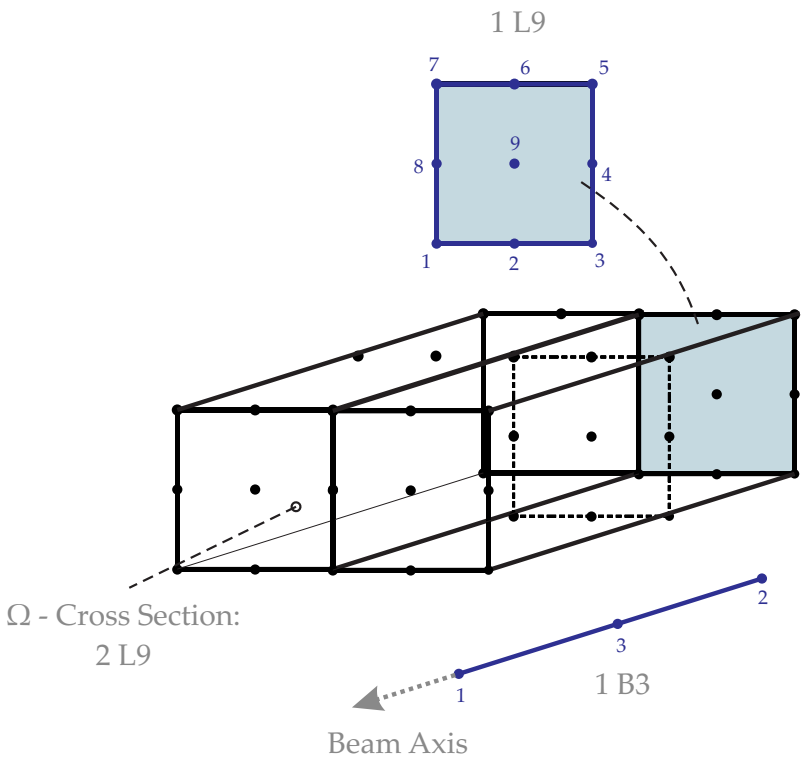

Figure 4.3. 3D Post-processing for the evaluation of integral parameters through the 1D LE CUF.

ment, it is necessary to define a volume in which to perform the integration starting from

the FE elements we have. This can actually being done if we consider the distribution in the frame (x,y,z) resulting from the CW approach as a cloud of nodes in a 3D space. In this case, the nodes lying on the cross-section will lie on the (x,z) plane while the nodes along the beam axis will lie along the y-axis of the frame. In Figure 4.3 is shown a cloud of nodes generated by the 2 L9 element nodes on the beam cross-section that are repeated at each beam node. At each node the three DOF u_x, u_y, u_z are known as well as the stress and strain fields. Considering the node distribution independently from the 1D FE perspective. It is possible to define 3D sub-domains for the integral computations. 3D 'fictitious' elements are identified into the cloud, depending on the picked nodes, where fictitious means that these elements are not actually used to perform a FEA. In particular, in this chapter three different fictitious elements equivalents to Brick 8, Brick 20 and Brick27 have been introduced to perform volume integrals in structural sub-domains. An example on how to identify these three different brick elements are respectively shown in 4.4, 4.5 and 4.6, These elements have different integration orders and use respectively 8-, 20- and 27-nodes. For each element, the shape functions used to carry the numerical informations on the Gauss points and compute integrals. Shape functions for the 8-nodes element are reported in Equation 4.9 while for the 20- and 27-nodes in Equations 4.11 and 4.3. Tables 4.1 4.2 and 4.3 shown the node coordinates in the natural frame. As in the analytical procedure the innermost integral is evaluated by keeping the variables corresponding to the other integrals constant. The numerical integration is performed using the Gauss quadrature as shown in the Equation 4.8. Using this numerical method, a polynomial of order $2n-1$ requires n function evaluations. Since Shape functions are written in the natural coordinate frame the physical coordinate system has to be introduced through the integral transformation as in Equation 4.5.

$$\int_V f(x,y,z)dxdydz = \int_N F(\xi,\eta,\nu)J(\xi,\eta,\nu)\partial\xi\partial\eta\partial\nu \tag{4.5}$$

where J, is the Jacobian Matrix:

$$[\boldsymbol{J}] = \begin{bmatrix} \frac{\partial\xi}{\partial x} & \frac{\partial\eta}{\partial x} & \frac{\partial\nu}{\partial x} \\ \frac{\partial\xi}{\partial y} & \frac{\partial\eta}{\partial y} & \frac{\partial\nu}{\partial y} \\ \frac{\partial\xi}{\partial z} & \frac{\partial\eta}{\partial z} & \frac{\partial\nu}{\partial z} \end{bmatrix} \tag{4.6}$$

and its determinant is used to transform the volume element from the cartesian coordinates to the natural coordinates as:

$$dxdydz = detJ\partial\xi\partial\eta\partial\nu \tag{4.7}$$

$$\int_{-1}^{+1}\int_{-1}^{+1}\int_{-1}^{+1} F(\xi,\eta,\nu)\partial\xi\partial\eta\partial\nu = \sum_{i,j,k}\alpha_i\alpha_j\alpha_k F(\xi_i,\eta_j,\nu_k) \tag{4.8}$$

where α_i, α_j, α_k are the integration weights. to be correctly integrated. Since the the function evaluations increase the computational time different fictitious 3D elements are created starting from the nodes lying along the beam (B-nodes) and on the cross section (L-nodes).

Point	ξ	η	ν
1	-1	-1	-1
2	1	-1	-1
3	1	1	-1
4	-1	1	-1
5	-1	-1	1
6	1	-1	1
7	1	1	1
8	-1	1	1

Table 4.1. Brick8 element point natural coordinates.

$$
\begin{aligned}
N_1 &= \tfrac{1}{8}\,[\,(1-\xi)\;(1-\eta)\;(1-\nu)] \\
N_2 &= \tfrac{1}{8}\,[\,(1+\xi)\;(1-\eta)\;(1-\nu)] \\
N_3 &= \tfrac{1}{8}\,[\,(1+\xi)\;(1+\eta)\;(1-\nu)] \\
N_4 &= \tfrac{1}{8}\,[\,(1-\xi)\;(1+\eta)\;(1-\nu)] \\
N_5 &= \tfrac{1}{8}\,[\,(1-\xi)\;(1-\eta)\;(1+\nu)] \\
N_6 &= \tfrac{1}{8}\,[\,(1+\xi)\;(1-\eta)\;(1+\nu)] \\
N_7 &= \tfrac{1}{8}\,[\,(1+\xi)\;(1+\eta)\;(1+\nu)] \\
N_8 &= \tfrac{1}{8}\,[\,(1-\xi)\;(1+\eta)\;(1+\nu)]
\end{aligned}
\tag{4.9}
$$

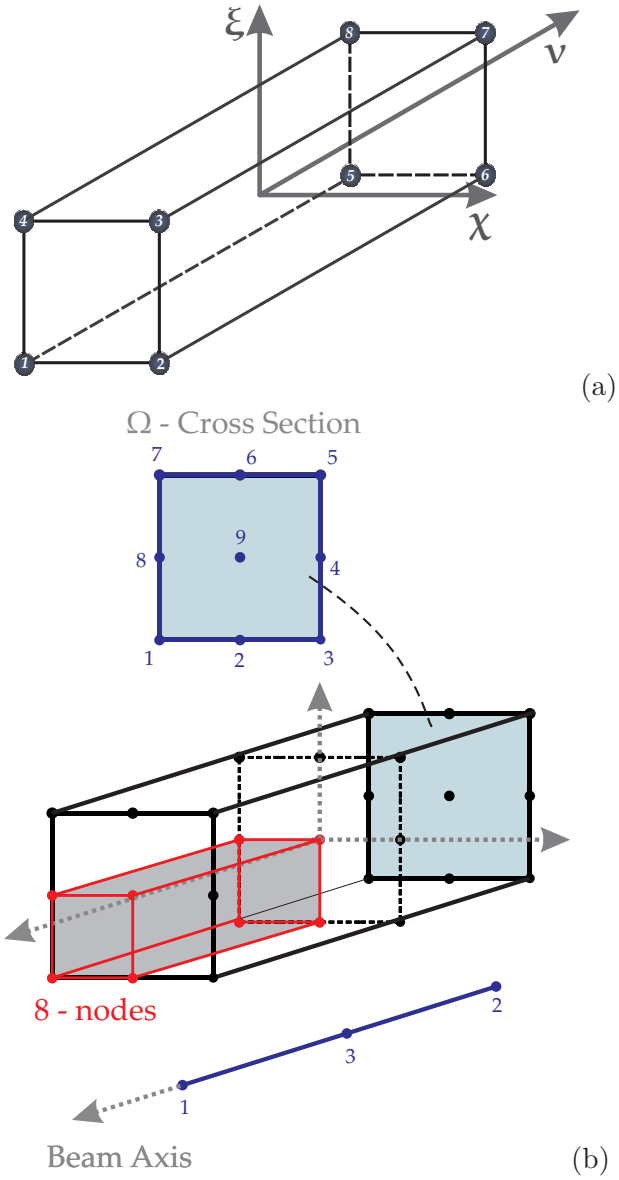

Figure 4.4. (a) 8 node hexahedral element coordinates in the natural reference frame. (b) 8 node element sub-domain in a 1D LE CUF model.

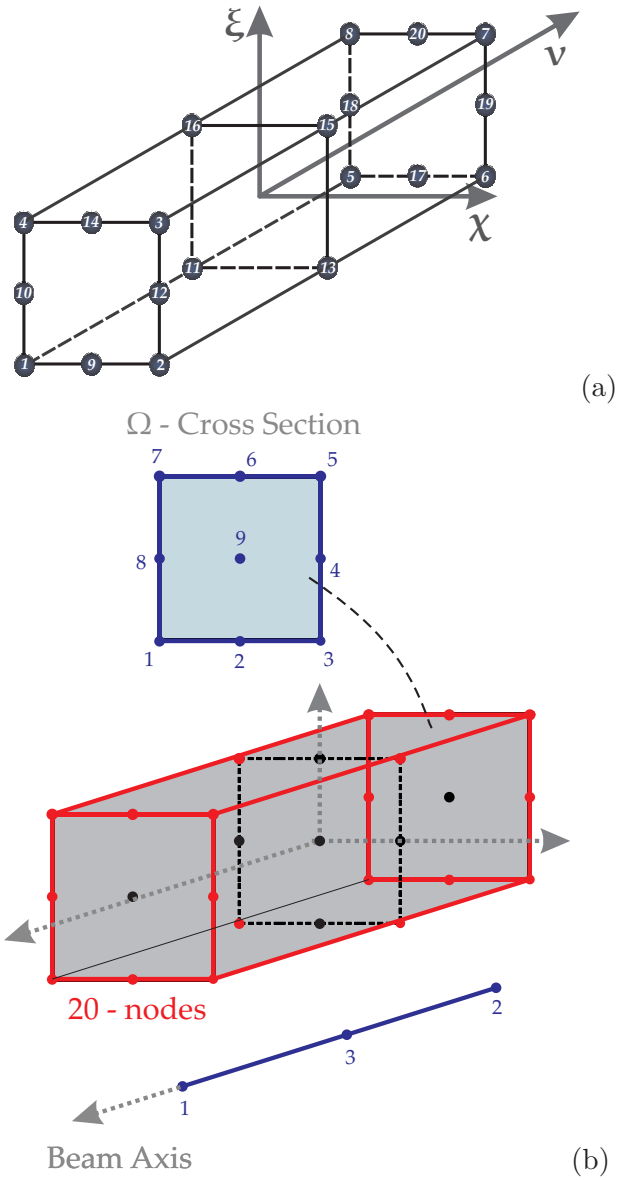

Figure 4.5. (a) 20 node hexahedral element coordinates in the natural reference frame. (b) 20 node element sub-domain in a 1D LE CUF model.

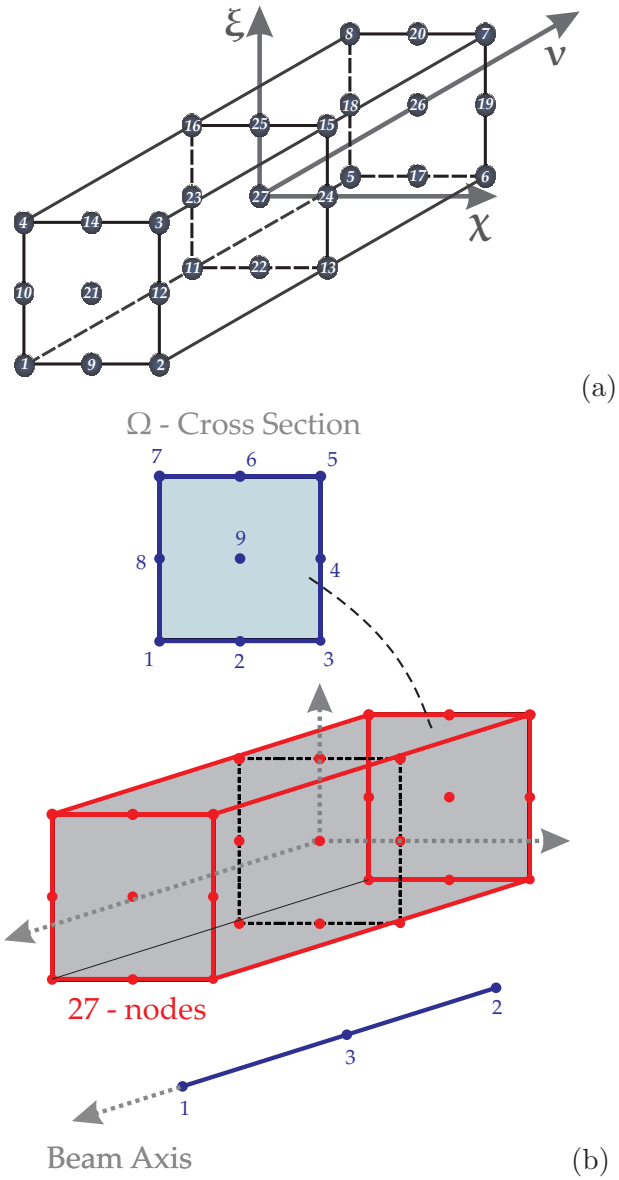

Figure 4.6. (a) 27 node hexahedral element coordinates in the natural reference frame. (b) 27 node element sub-domain in a 1D LE CUF model.

Point	ξ	η	ν
1	-1	-1	-1
2	1	-1	-1
3	1	1	-1
4	-1	1	-1
5	-1	-1	1
6	1	-1	1
7	1	1	1
8	-1	1	1
9	0	-1	-1
10	-1	0	-1
11	-1	-1	0
12	1	0	-1
13	1	-1	0
14	0	1	-1
15	1	1	0
16	-1	1	0
17	0	-1	1
18	-1	0	1
19	1	0	1
20	0	1	1

Table 4.2. Brick20 element point natural coordinates.

$$
\begin{aligned}
N_1 &= \tfrac{1}{8}\left[\,(1-\xi)\;(1-\eta)\;(1-\nu)\right]\;(-\xi-\nu-\eta-2)\\
N_2 &= \tfrac{1}{8}\left[\,(1+\xi)\;(1-\eta)\;(1-\nu)\right]\;(\xi-\nu-\eta-2)\\
N_3 &= \tfrac{1}{8}\left[\,(1+\xi)\;(1+\eta)\;(1-\nu)\right]\;(-\xi-\nu+\eta-2)\\
N_4 &= \tfrac{1}{8}\left[\,(1-\xi)\;(1+\eta)\;(1-\nu)\right]\;(-\xi-\nu+\eta-2)\\
N_5 &= \tfrac{1}{8}\left[\,(1-\xi)\;(1-\eta)\;(1+\nu)\right]\;(-\xi+\nu-\eta-2)\\
N_6 &= \tfrac{1}{8}\left[\,(1+\xi)\;(1-\eta)\;(1+\nu)\right]\;(\xi+\nu-\eta-2)\\
N_7 &= \tfrac{1}{8}\left[\,(1+\xi)\;(1+\eta)\;(1+\nu)\right]\;(\xi+\nu+\eta-2)\\
N_8 &= \tfrac{1}{8}\left[\,(1-\xi)\;(1+\eta)\;(1+\nu)\right]\;(-\xi+\nu+\eta-2)\\
N_9 &= \tfrac{1}{4}\left[\,\left(1-\xi^2\right)\;(1-\eta)\;(1-\nu)\right]\\
N_{10} &= \tfrac{1}{4}\left[\,(1-\xi)\;\left(1-\eta^2\right)\;(1-\nu)\right]\\
N_{11} &= \tfrac{1}{4}\left[\,(1-\xi)\;(1-\eta)\;\left(1-\nu^2\right)\right]\\
N_{12} &= \tfrac{1}{4}\left[\,(1+\xi)\;\left(1-\eta^2\right)\;(1-\nu)\right]\\
N_{13} &= \tfrac{1}{4}\left[\,(1+\xi)\;(1-\eta)\;\left(1-\nu^2\right)\right]\\
N_{14} &= \tfrac{1}{4}\left[\,\left(1-\xi^2\right)\;(1+\eta)\;(1-\nu)\right]\\
N_{15} &= \tfrac{1}{4}\left[\,(1+\xi)\;(1+\eta)\;\left(1-\nu^2\right)\right]\\
N_{16} &= \tfrac{1}{4}\left[\,(1-\xi)\;(1+\eta)\;\left(1-\nu^2\right)\right]\\
N_{17} &= \tfrac{1}{4}\left[\,\left(1-\xi^2\right)\;(1-\eta)\;(1+\nu)\right]\\
N_{18} &= \tfrac{1}{4}\left[\,(1-\xi)\;\left(1-\eta^2\right)\;(1+\nu)\right]\\
N_{19} &= \tfrac{1}{4}\left[\,(1+\xi)\;\left(1-\eta^2\right)\;(1+\nu)\right]\\
N_{20} &= \tfrac{1}{4}\left[\,\left(1-\xi^2\right)\;(1+\eta)\;(1+\nu)\right]
\end{aligned}
\tag{4.10}
$$

$$
\begin{aligned}
N_1 &= \tfrac{1}{8}\left[\left(\xi^2-\xi\right)\ \left(\eta^2-\eta\right)\ \left(\nu^2-\nu\right)\right]\\
N_2 &= \tfrac{1}{8}\left[\left(\xi^2+\xi\right)\ \left(\eta^2-\eta\right)\ \left(\nu^2-\nu\right)\right]\\
N_3 &= \tfrac{1}{8}\left[\left(\xi^2+\xi\right)\ \left(\eta^2+\eta\right)\ \left(\nu^2-\nu\right)\right]\\
N_4 &= \tfrac{1}{8}\left[\left(\xi^2-\xi\right)\ \left(\eta^2+\eta\right)\ \left(\nu^2-\nu\right)\right]\\
N_5 &= \tfrac{1}{8}\left[\left(\xi^2-\xi\right)\ \left(\eta^2-\eta\right)\ \left(\nu^2+\nu\right)\right]\\
N_6 &= \tfrac{1}{8}\left[\left(\xi^2+\xi\right)\ \left(\eta^2-\eta\right)\ \left(\nu^2+\nu\right)\right]\\
N_7 &= \tfrac{1}{8}\left[\left(\xi^2+\xi\right)\ \left(\eta^2+\eta\right)\ \left(\nu^2+\nu\right)\right]\\
N_8 &= \tfrac{1}{8}\left[\left(\xi^2-\xi\right)\ \left(\eta^2+\eta\right)\ \left(\nu^2+\nu\right)\right]\\
N_9 &= \tfrac{1}{4}\left[\left(1-\xi^2\right)\ \left(\eta^2-\eta\right)\ \left(\nu^2-\nu\right)\right]\\
N_{10} &= \tfrac{1}{4}\left[\left(\xi^2-\xi\right)\ \left(1-\eta^2\right)\ \left(\nu^2-\nu\right)\right]\\
N_{11} &= \tfrac{1}{4}\left[\left(\xi^2-\xi\right)\ \left(\eta^2-\eta\right)\ \left(1-\nu^2\right)\right]\\
N_{12} &= \tfrac{1}{4}\left[\left(\xi^2+\xi\right)\ \left(1-\eta^2\right)\ \left(\nu^2-\nu\right)\right]\\
N_{13} &= \tfrac{1}{4}\left[\left(\xi^2+\xi\right)\ \left(\eta^2-\eta\right)\ \left(1-\nu^2\right)\right]\\
N_{14} &= \tfrac{1}{4}\left[\left(\eta^2+\eta\right)\ \left(\eta^2-\eta\right)\ \left(1-\nu^2\right)\right]\\
N_{15} &= \tfrac{1}{4}\left[\left(1-\xi^2\right)\ \left(\eta^2+\eta\right)\ \left(\nu^2-\nu\right)\right]\\
N_{16} &= \tfrac{1}{4}\left[\left(\xi^2+\xi\right)\ \left(\eta^2+\eta\right)\ \left(1-\nu^2\right)\right]\\
N_{17} &= \tfrac{1}{4}\left[\left(\xi^2-\xi\right)\ \left(\eta^2+\eta\right)\ \left(1-\nu^2\right)\right]\\
N_{18} &= \tfrac{1}{4}\left[\left(1-\xi^2\right)\ \left(\eta^2-\eta\right)\ \left(\nu^2+\nu\right)\right]\\
N_{19} &= \tfrac{1}{4}\left[\left(\xi^2-\xi\right)\ \left(1-\eta^2\right)\ \left(\nu^2+\nu\right)\right]\\
N_{20} &= \tfrac{1}{4}\left[\left(\xi^2+\xi\right)\ \left(1-\eta^2\right)\ \left(\nu^2+\nu\right)\right]\\
N_{21} &= \tfrac{1}{2}\left[\left(1-\xi^2\right)\ \left(\eta^2+\eta\right)\ \left(\nu^2+\nu\right)\right]\\
N_{22} &= \tfrac{1}{2}\left[\left(1-\xi^2\right)\ \left(\eta^2-\eta\right)\ \left(1-\nu^2\right)\right]\\
N_{23} &= \tfrac{1}{2}\left[\left(\xi^2-\xi\right)\ \left(1-\eta^2\right)\ \left(1-\nu^2\right)\right]\\
N_{24} &= \tfrac{1}{2}\left[\left(\xi^2+\xi\right)\ \left(1-\eta^2\right)\ \left(1-\nu^2\right)\right]\\
N_{25} &= \tfrac{1}{2}\left[\left(1-\xi^2\right)\ \left(\eta^2+\eta\right)\ \left(1-\nu^2\right)\right]\\
N_{26} &= \tfrac{1}{2}\left[\left(1-\xi^2\right)\ \left(1-\eta^2\right)\ \left(\nu^2+\nu\right)\right]\\
N_{27} &= \tfrac{1}{2}\left[\left(1-\xi^2\right)\ \left(1-\eta^2\right)\ \left(1-\nu^2\right)\right]
\end{aligned}
\tag{4.11}
$$

4.2.2 Homogeneous Square Cell

For the homogeneous case study, in order to validate the estimation of the integral parameter, results are compared with those of a solid model built using 20-node solid elements. In Figure 4.7 the two employed meshes are provided respectively for the CW model and

Point	ξ	η	ν
1	-1	-1	-1
2	1	-1	-1
3	1	1	-1
4	-1	1	-1
5	-1	-1	1
6	1	-1	1
7	1	1	1
8	-1	1	1
9	0	-1	-1
10	-1	0	-1
11	-1	-1	0
12	1	0	-1
13	1	-1	0
14	0	1	-1
15	1	1	0
16	-1	1	0
17	0	-1	1
18	-1	0	1
19	1	0	1
20	0	1	1
21	0	0	-1
22	0	-1	0
23	-1	0	0
24	1	0	0
25	0	1	0
26	0	0	1
27	0	0	0

Table 4.3. Brick27 element point natural coordinates.

for the solid model, where the first and the last subvolumes taken into account are highlighted in red. The CW mesh is obtained through one nine-points (L9) element on the cross-section and 30 B3 elements along the y-axis. The structure is clamped at one end and four bending forces are applied at the free-tip corners as depicted, F = 0.025 N. In Table 4.4 results are shown in terms of strain energy, the first column provides CW model results while in the second column solid results are reported. Results show that for each subvolumes the strain energy can be evaluated with solid like accuracy with a reduced computational cost. In fact, as shown in the last row of the table, the CW approach has almost 3 times less DOFs. Then, a further subdivision in 30 subvolumes was taken into account. Through this second subdivision, it was possible to catch the local effect of the loading in Figure 4.8 where the strain energy distribution along the beam axis is depicted.

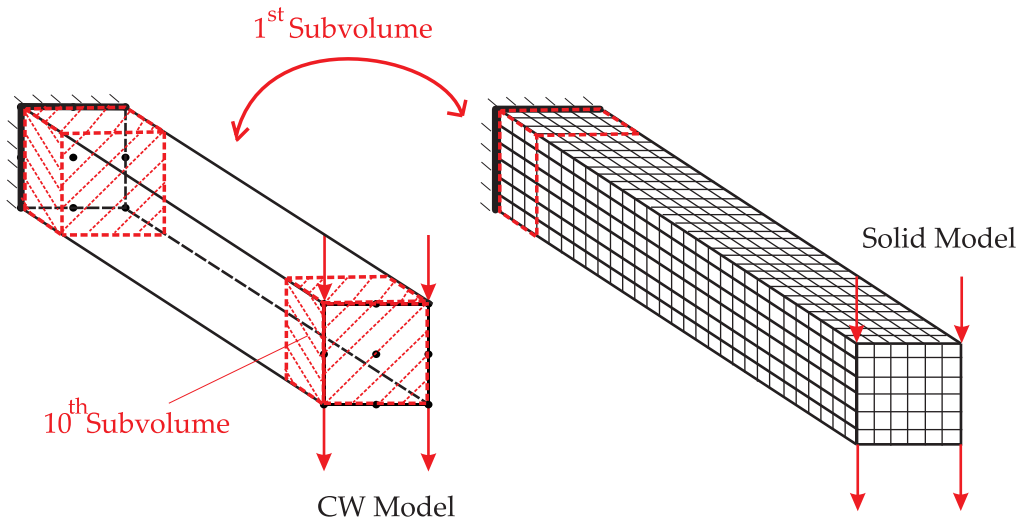

Figure 4.7. CW and Solid Models for the homogeneous assessment.

	E_i [mJ]	
Vol	CW	Solid
	$\times 10^4$	
1	1.030	1.023
	E $\times 10^5$	
2	8.529	8.535
3	6.648	6.651
4	5.002	5.006
5	3.592	3.595
6	2.416	2.420
7	1.476	1.479
	$\times 10^6$	
8	7.703	7.738
9	3.000	3.036
10	1.301	1.470
	E $\times 10^4$ [mJ]	
Tot	3.917	3.914
	DOFs	
	1647	4557

Table 4.4. Strain energy distribution in homogeneous beam subvolumes.

4.2.3 Single Fiber/Matrix cell

In the CW perspective the simplest structural layout is a fiber/matrix cell. Figure 4.9 provides a graphic description of a possible approach to perform the evaluation of integrals parameters for the single cell case study. A typical strategy can be based on a preliminary volume subdivision at macroscale. Where deemed appropriate, components can be identified and finer subvolume distributions can be considered up to the fiber and matrix portions dimension. Fiber and matrix volumes are evaluated with their own properties. The analyzed cell is square with side h = 0.1 mm, and L/h = 10 where L is the longitudinal length of the structure. The fiber diameter is d = 0.08 mm. The mesh is obtained by means of 10 B3 elements along the y-axis and 20 L9 elements on the cross-section. The structure is clamped at y = 0. Two loading configurations are analyzed as shown in Figure 4.10. In a first case study, four bending force are locally applied on the matrix at the cell corners, F = 0.025 N. Then, in a second case two torsional loading forces, F = 0.05 N, are applied at [0, L, h/2] and [h, L, h/2]. For the evaluation of the integral quantities two main subvolumes of the whole structure are considered as depicted in Figure 4.11 where, the first is indicated as 1/2 and the last with 2/2.

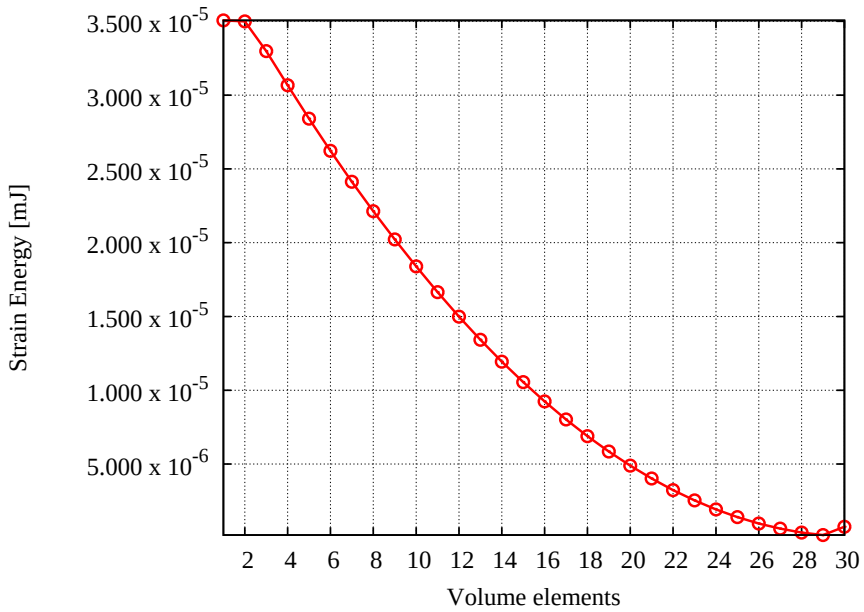

Figure 4.8. Strain energy distribution along the y-axis.

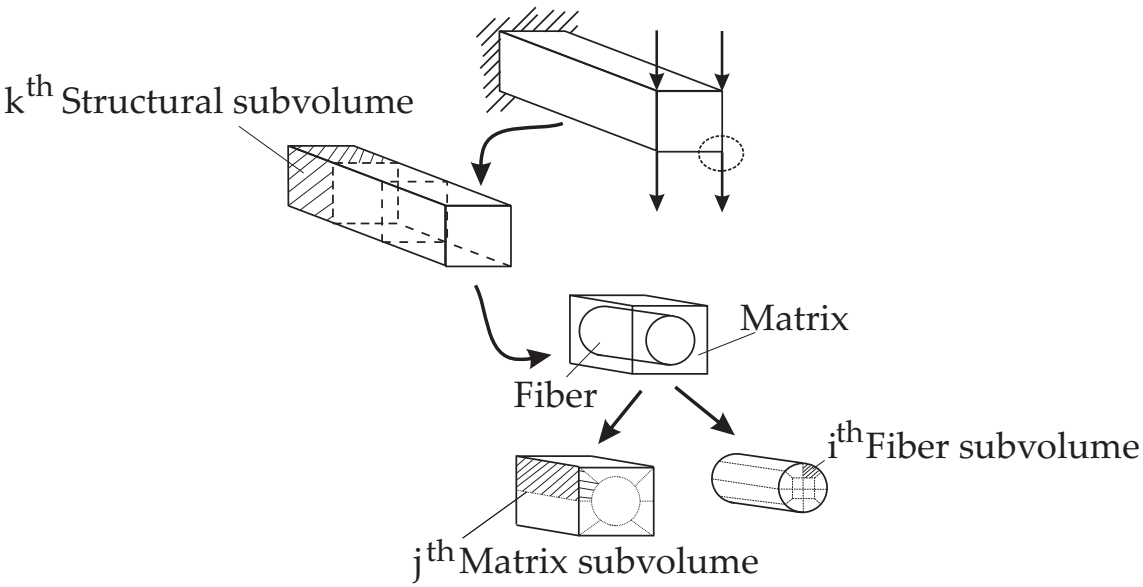

Figure 4.9. Component-Wise approach for volume evaluations.

Results of this preliminary investigation are provided in Table 4.5 in terms of the total strain energy E, axial strain energy E_{ax} and shear strain energy E_s. Furthermore, the strain energy of each subvolume, E_i, is normalized with respect to the strain energy of the whole model, E. Axial ($E_{ax,i}$) and shear ($E_{s,i}$) strain energies respectively normalized to the axial E_{ax} and the shear E_s strain energy of the whole structure are also take into

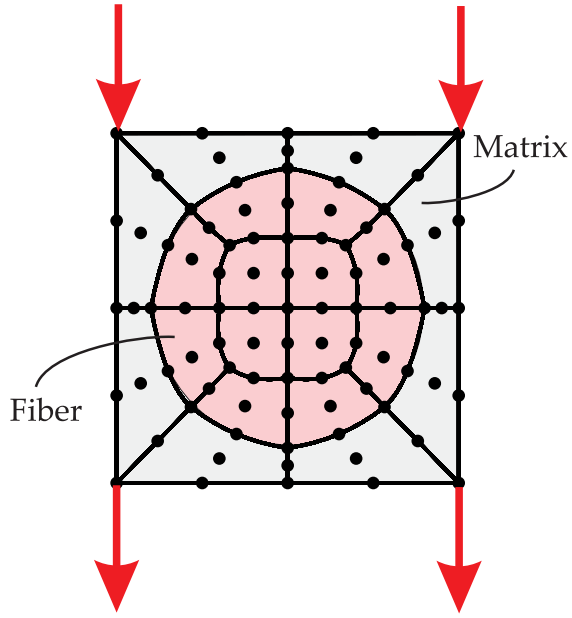

(a) Bending loading case

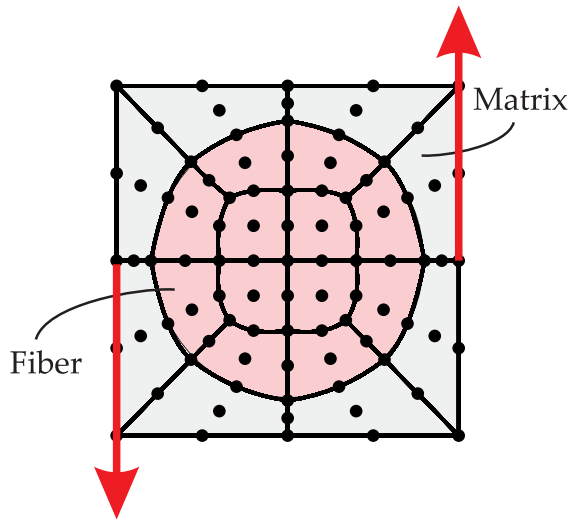

(b) Torsion loading case

Figure 4.10. Loading configurations.

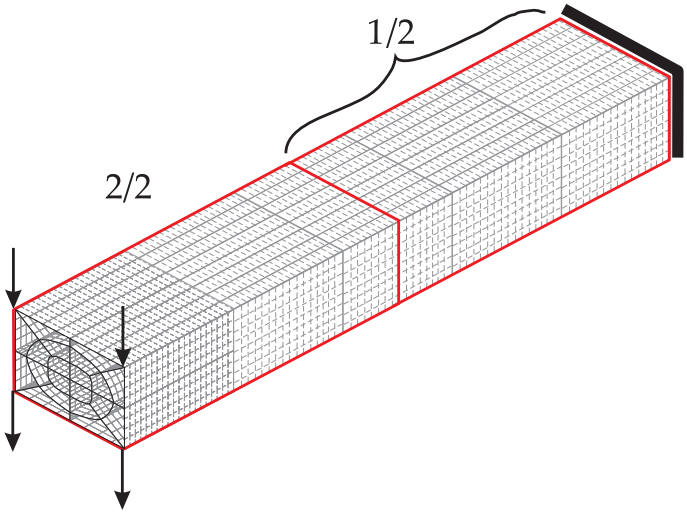

Figure 4.11. First subvolume distributions.

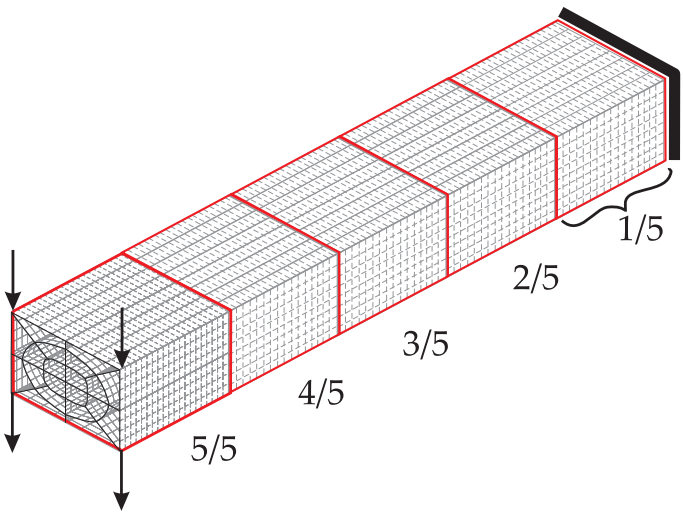

Figure 4.12. Second subvolume distributions.

account. This preliminary analysis shows that the main part of the total and axial strain energy of the cell due to the bending are localized around the clamp, while for the the shear strain energy is around the free tip while for the torsion load the main part of the energy is absorbed by the second subvolume. Then, a further subvolume distribution is analyzed, five parts of the structure are considered as depicted in Figure 4.12. In this second volume distribution, numerical results show that $E_{i,max}$ and $E_{ax,max}$ are in the first subvolume, while $E_{s,max}$ is in the fifth subvolume for the bending load. For the torsion case the fifth subvolume appear to be the most stressed. Furthermore, CW approach is able to distinguish the component strain energies to determine what is the contribution

	Bending			Torsion	
Vol	E_i/E	$E_{ax,i}/E_{ax}$	$E_{s,i}/E_s$	E_i/E	$E_{s,i}/E_s$
1/2	**0.846**	**0.874**	0.308	0.138	0.415
2/2	0.154	0.126	**0.692**	**0.862**	**0.585**
1/5	**0.469**	**0.484**	0.177	0.055	0.168
2/5	0.289	0.298	0.089	0.055	0.166
3/5	0.149	0.153	0.082	0.055	0.163
4/5	0.055	0.056	0.083	0.056	0.169
5/5	0.038	0.008	**0.568**	**0.778**	**0.334**
	$E \times 10^3$ [mJ]	$E_{ax} \times 10^3$ [mJ]	$E_s \times 10^5$ [mJ]	$E \times 10^4$ [mJ]	$E_s \times 10^5$ [mJ]
	3.448	3.331	3.257	1.150	3.775

Table 4.5. Strain Energy in beam subvolumes.

given by the fiber and by the matrix. In Table 4.6 results are shown for the bending load. The superscrits "f" and "m" respectively refer to fiber and matrix. CW approach shows that in this load configuration, the main axial strain energy is absorbed by the fiber while the matrix mainly absorbs the shear strain energy. Table 4.8 reports results for

Single cell: bending			
		Matrix	
Vol	$E^m_{,i}/E^m$	$E^m_{ax,i}/E^m_{ax}$	$E^m_{s,i}/E^m$
1/2	**0.509**	**0.872**	0.046
2/2	0.491	0.128	**0.954**
1/5	**0.275**	**0.488**	0.039
2/5	0.171	0.293	0.005
3/5	0.088	0.151	0.004
4/5	0.033	0.056	0.008
5/5	0.423	0.012	**0.945**
	$E^m \times 10^4$ [mJ]	$E^m_{ax} \times 10^4$ [mJ]	$E^m_s \times 10^5$ [mJ]
	2.468	1.449	1.688

Table 4.6. Strain Energy the matrix subvolumes.

the torsion loading case. For both cases, in the last fifth (5/5) it is possible to detect the local effect on the matrix due to the loading. Focusing on the sixteen subvolumes shown in Figure 4.13, the strain energy at the microscale can be evaluated. Table 4.9 reports that the bending loading has more effect on the matrix subvolumes 9-16 while the torsion loading affects principally the subvolumes 11-12,15-16. On the basis of the stress and strain distribution well known criteria are usually employed to detect the failure initiation. The criteria identify an index, FI, referred to as Failure Index, that becomes the parameter that determines the failure initiation. Points in which the index becomes greater or equal

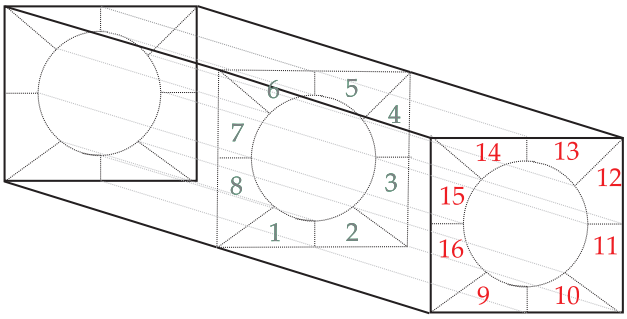

Figure 4.13. Matrix subvolumes near the free tip.

Single cell: bending			
	Fiber		
Vol	$E^f_{,i}/E^f$	$E^f_{ax,i}/E^f_{ax}$	$E^f_{s,i}/E^f_s$
1/2	**0.873**	**0.874**	**0.591**
2/2	0.127	0.126	0.409
1/5	**0.483**	**0.484**	**0.326**
2/5	0.298	0.298	0.180
3/5	0.153	0.153	0.167
4/5	0.057	0.056	0.164
5/5	0.009	0.008	0.162
	$E^f \times 10^3$ [mJ]	$E^f_{ax} \times 10^3$ [mJ]	$E^f_s \times 10^5$ [mJ]
	3.201	3.186	1.569

Table 4.7. Strain Energy in the fiber subvolumes.

Single cell: torsion				
	Fiber		Matrix	
Vol	$E^f_{,i}/E^f$	$E^f_{s,i}/E^f_s$	$E^m_{,i}/E^m$	$E^m_{s,i}/E^m_s$
1/2	0.501	0.506	0.006	0.042
2/2	0.499	0.494	**0.994**	**0.958**
1/5	0.200	0.202	0.002	0.028
2/5	0.200	0.203	0.002	0.014
3/5	0.200	0.203	0.002	0.000
4/5	0.200	0.202	0.003	0.032
5/5	0.199	0.190	**0.989**	**0.925**
	$E^f \times 10^5$ [mJ]	$E^f_s \times 10^5$ [mJ]	$E^m \times 10^5$ [mJ]	$E^m_s \times 10^6$ [mJ]
	3.069	3.035	8.436	7.399

Table 4.8. Strain Energy in fiber and matrix subvolumes.

to one indicate the failure. In this work two failure criteria are employed: the Maximum Stress (MS) and Tsai-Wu (TW) criteria. Failure index distributions for both criteria at clamped cross-section, are shown in Figure 4.14 for the bending case study where, failure occurs in the bottom portion of the fiber. Integral results are given in terms of FI^* for both the loading case studies in Table 4.10. Subvolume criticalities change depending on the load configurations. The failure parameter FI^* is evaluated on fiber and matrix, approximations introduced by the homogenization theories are avoided.

	Bending		Torsion	
Vol ID	$E^m_{,j}/E^{m*}$	$E^m_{s,j}/E^{m*}$	$E^m_{,j}/E^{m*}$	$E^m_{s,j}/E^{m*}$
1	0.004	0.006	0.000	0.003
2	0.004	0.006	0.000	0.003
3	0.003	0.003	0.006	0.014
4	0.003	0.003	0.006	0.014
5	0.004	0.006	0.000	0.003
6	0.004	0.006	0.000	0.003
7	0.003	0.003	0.006	0.014
8	0.003	0.003	0.006	0.014
9	0.079	0.123	0.003	0.013
10	0.079	0.123	0.003	0.013
11	0.164	0.117	0.241	0.220
12	0.164	0.117	0.241	0.220
13	0.079	0.123	0.003	0.013
14	0.079	0.123	0.003	0.013
15	0.164	0.117	0.241	0.220
16	0.164	0.117	0.241	0.220

Table 4.9. Local Effect on matrix due to the bending loads.

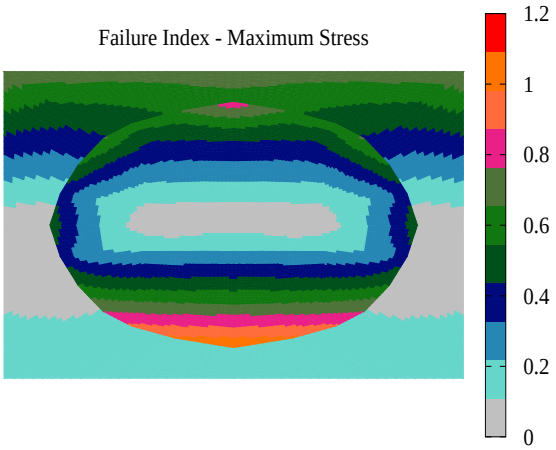

(a)

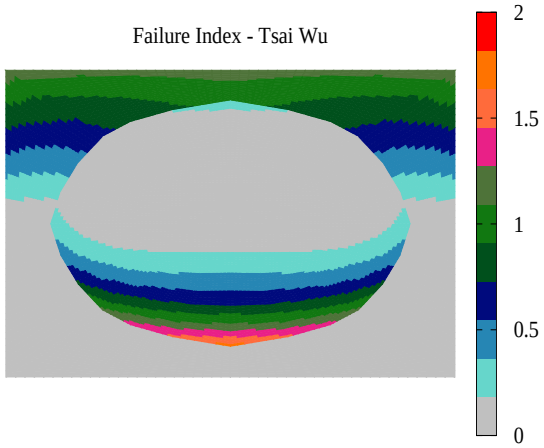

(b)

Figure 4.14. Maximum Stress (MS) and Tsai-Wu (TW) Failure indexes over the single cell clamped cross-section under bending loading.

	Bending				Torsion			
	Fiber		Matrix		Fiber		Matrix	
Vol	FI* TW	FI* MS	FI* TW	FI* MS	FI* TW	FI* MS	FI* TW	FI* MS
	0.070	0.124	0.010	0.050	0.073	0.095	0.008	0.009
1/2	0.097	0.163	0.006	0.063	0.074	0.096	0.000	0.003
2/2	0.044	0.086	0.014	0.036	0.073	0.094	0.016	0.014
1/5	0.129	0.190	0.007	0.077	0.074	0.096	0.000	0.003
2/5	0.082	0.153	0.006	0.058	0.074	0.096	0.000	0.003
3/5	0.058	0.119	0.003	0.042	0.074	0.096	0.000	0.003
4/5	0.043	0.089	0.001	0.025	0.074	0.096	0.000	0.004
5/5	0.039	0.069	0.032	0.046	0.072	0.092	0.041	0.029

Table 4.10. Failure index integrated over the subvolumes normalized with respect to the number of subvolumes.

4.2.4 Laminate

The CW approach appears to be attractive in the perspective of a detailed analysis of complex structural configurations. Cells can be opportunely included in order to refine the model in areas that were considered critical following preliminary analyses. Once determined the portion of the structure that is working in the worst condition a model that includes components can be analyzed. Possible subvolumes are depicted in Figure 4.15 for a three layers laminate. Two different case studies are herein proposed: laminate (a) and (b). Respectively, one single fiber/matrix cell is included in the first lamina then, an entire row of cells are taken into account.
The structural analysis of a cantilever laminated beam is herein proposed. Stacking sequence of the plies is [0/90/0]. The height (h) and the width (b) are equal to 0.6 mm and 0.8 mm, respectively. L/h = 10. For each layer h_i = 0.2 mm. A fiber/matrix cell is modeled as having a geometry of the previous analyzed cell. The structure is clamped at y = 0. For the fist case study, laminate (a), two loading configurations are analyzed. First, a bending force is locally applied on the center of the second lamina as shown in Figure 4.16, F = 5 N. Then, four torsion forces, F = 1 N, are applied. The mesh is obtained by means of 15 B3 elements along the y-axis and 41 L9 elements on the cross-section as depicted in Figure 4.17 where are also shown the torsional forces. Results in terms of axial stress σ_{yy} are provided for both loading configurations 4.18. In this structural configuration, the three layers are chosen as main subvolumes. Results are shown in Table 4.12 and 4.11 in terms of strain energy. It is possible to observe that in the bending load configuration the first and the third lamina absorb the main part of the axial strain energy while the second absorb the 77,2% of the shear strain energy. Torsion loading determines a mainly equal redistribution of the strain energy. Furthermore it is possible to evaluate the strain energy absorbed by the cell included. Tables 4.14 and 4.13 shows the total amount of energy absorbed, the total, axial and strain energy normalized with respect to

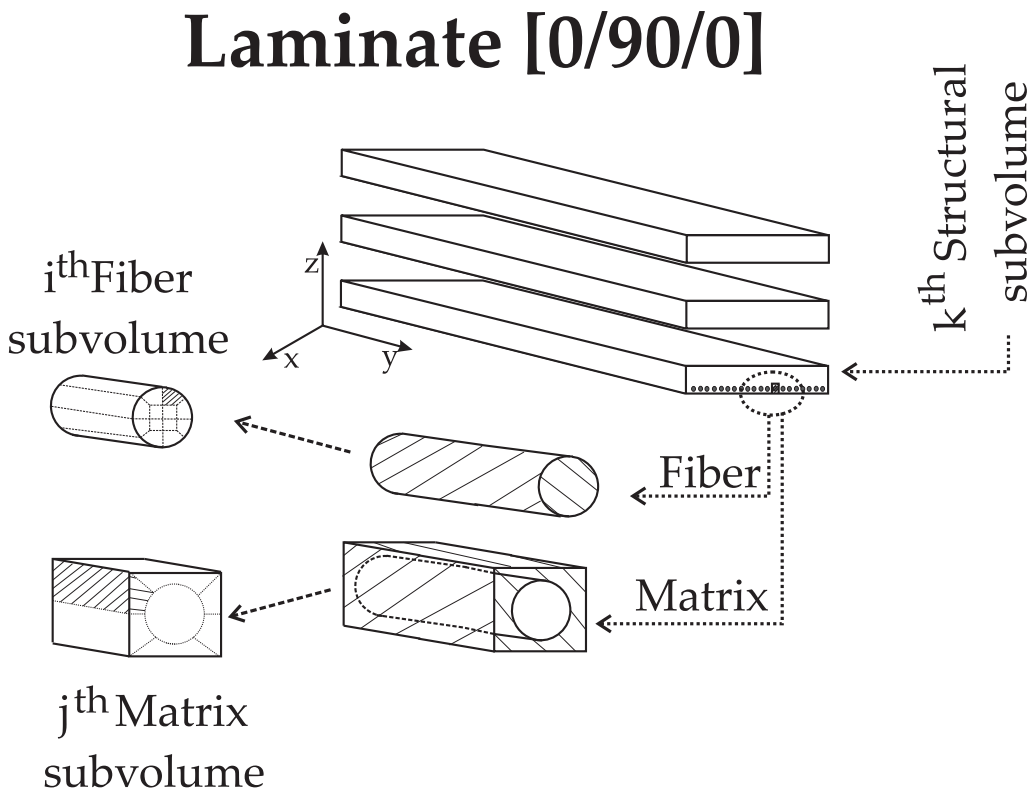

Figure 4.15. Component-Wise approach for subvolume evaluations.

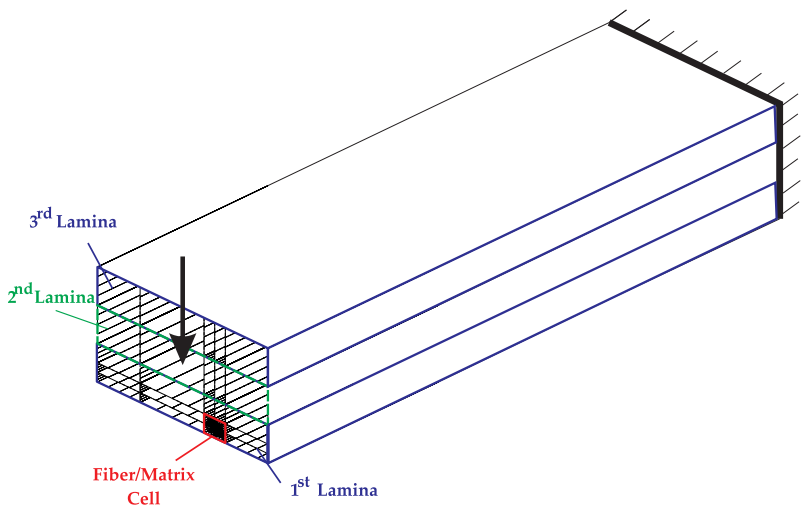

Figure 4.16. First laminated beam mode - laminate (a).